SUPERGRANULATION AS THE LARGEST BUOYANTLY DRIVEN CONVECTIVE SCALE OF THE SUN

JEAN-FRANCOIS COSSETTE[1] AND MARK P. RAST[2]
[1] Laboratory for Atmospheric and Space Physics, University of Colorado, Boulder, CO, USA
[2] Department of Astrophysical and Planetary Sciences, Laboratory for Atmospheric and Space Physics, University of Colorado, Boulder, CO, USA

ABSTRACT

The origin of solar supergranulation remains a mystery. Unlike granulation, the size of which is comparable to both the thickness of the radiative boundary layer and local scale-height in the photosphere, supergranulation does not reflect any obvious length scale of the solar convection zone. Moreover, recent observations of flows in the photosphere using Doppler imaging or correlation or feature tracking show a monotonic decrease in horizontal flow power at scales larger than supergranulation. Both local area and global spherical shell simulations of solar convection by contrast show the opposite, an increase in horizontal flow amplitudes to a low wavenumber. We examine these disparities and investigate how the solar supergranulation may arise as a consequence of nonlocal heat transport by cool diving plumes. Using three-dimensional anelastic simulations with surface driving, we show that the kinetic energy of the largest convective scales in the upper layers of a stratified domain reflects the depth of transition from strong buoyant driving to adiabatic stratification below caused by the dilution of the granular downflows. This depth is quite shallow because of the rapid increase of the mean density below the photosphere. We interpret the observed monotonic decrease in solar convective power at scales larger than supergranulation to be a consequence of this rapid transition, with the supergranular scale the largest buoyantly driven mode of convection in the Sun.

Key words: Sun: interior

1. INTRODUCTION

Solar convective scales include granules, mesogranules, and supergranules, with recent observations hinting at the possibility of giant cells (Hathaway et al. 2013). Granules (about 1 Mm diameter and 0.2 hr lifetime) are the signature of convection driven in the highly superadiabatic layers of the photosphere. Direct observation in continuum intensity images has confirmed their convective nature via the correlation of vertical velocity with intensity (e.g., Nordlund et al. 2009). Supergranules (about 32 Mm diameter and 1.8 day lifetime) are observed largely as a horizontal flow using either Doppler imaging, magnetic feature or granule tracking, or local helioseismology (Hanasoge et al. 2016). The horizontally divergent motion and cellular nature of supergranulation suggest a convective origin (Goldbaum et al. 2009). The physical mechanism responsible for supergranulation remains unclear. The early suggestion that the second ionization of helium plays an important role (Leighton et al. 1962; Simon & Leighton 1964; November et al. 1981) is not supported by numerical simulation (Rast & Toomre 1993; Lord et al. 2014), while the later suggestion that supergranulation results from self-organization of granular flows (Rieutord et al. 2000; Rast 2003; Crouch et al. 2007) may be more relevant on mesogranular scales (Cattaneo et al. 2001; Berrilli et al. 2005; Leitzinger et al. 2005; Duvall & Birch 2010). The existence of mesogranules (about 5 Mm diameter and 3 hr lifetime; November et al. 1981) as a real convective feature distinct from both granules and supergranules is still debated (November 1989; Berrilli et al. 2013).

Convective structures much larger than supergranules, including so-called giant cells, are predicted by both mixing length theories and global models of solar convection (Christensen-Dalsgaard et al. 1996; Miesch et al. 2008). However, observations suggest that the velocities associated with these large-scale motions are significantly weaker than predicted. Time–distance helioseismology provides the most severe constraint, with large-scale velocity amplitudes at 28–56 Mm depth measured to be orders of magnitude smaller than in models (Hanasoge et al. 2010, 2012). However, ring diagram helioseismic analysis does not confirm this, instead showing at 30 Mm depth a continuous increase of power to scales larger than supergranulation, in good agreement with numerical experiments (Greer et al. 2015). Where models and observations most fundamentally disagree is in the surface layers. Horizontal velocity power spectra obtained from Doppler imaging and correlation tracking of flow features at the solar surface reveal peaks corresponding to granular (angular harmonic degree $l \sim 3500$) and supergranular scales ($l \sim 120$), followed by a monotonic decrease in power to larger scales (Hathaway et al. 2000; Roudier et al. 2012; Hathaway et al. 2015). In contrast, radiative hydrodynamic and magneto-hydrodynamic local area models of solar photospheric convection show, as the global models, horizontal power increasing to scales larger than supergranulation (Lord et al. 2014; Hanasoge et al. 2016).

This discrepancy between modeled and observed power may be related to the difficulties global models have reproducing a solar-like differential rotation in the parameter regime characteristic of the solar interior. Models indicate that rotationally constrained giant cells, which transport angular momentum toward the equator, are essential in maintaining the prograde equatorial differential rotation (e.g., Miesch et al. 2008) observed at the photosphere and in accordance with the angular velocity profiles inferred from helioseismology (Thompson et al. 2003). These solar-like states are achieved when the flow is rotationally constrained, when the influence of the Coriolis force dominates over the flow's inertia, which places an upper limit on the convective flow speeds. This upper limit is weaker than the flow amplitudes required to transport the solar luminosity in global simulations (e.g., Hotta

et al. 2015). Moreover, as numerical diffusivities are lowered, the flows become more turbulent and velocity fields tend to decorrelate, which can lead to faster convective motions and retrograde (poles rotating faster than the equator) rather than prograde differential rotation (Gastine et al. 2013; Featherstone & Miesch 2015). Models of the Sun's convection can reproduce global scale motions only if the flux through the domain is reduced or the rotation rate of the star is increased.

These difficulties suggest that global motions in the Sun are weak enough to be rotationally constrained, with smaller scales carrying the convective flux (Lord et al. 2014; Featherstone & Hindman 2016; O'Mara et al. 2016). One possible solution to the conundrum is that the mean entropy gradient in the deep convection zone is closer to adiabatic than that achieved in most simulations, limiting convective driving below the surface and leading to a horizontal velocity spectrum in the photosphere consistent with that observed (Lord et al. 2014). It implies that the solar supergranulation reflects the largest buoyantly driven convective scale of the Sun.

In this Letter, we use 3D numerical simulations of solar convection to assess how this might be achieved. We investigate vigorously driven surface convection and determine how downflowing plumes alter the mean state as they descend through initially adiabatically stratified fluid below. We examine the spectra that result and show that they are dependent on the rate of the transition to adiabatic stratification and that, when the transit time of the fluid parcels across the convection zone is much shorter than the diffusion time, the depth of that transition depends only on the entropy contrast of the downflows and the change in mean density with depth.

2. MODEL

We simulate solar hydrodynamic convection by solving the Lipps & Hemler (1982) version of the anelastic Euler equations governing the evolution of momentum and entropy perturbations in a gravitationally stratified fluid:

$$\frac{D\boldsymbol{u}}{Dt} = -\nabla\pi' + g\frac{\Theta'}{\Theta_o}\boldsymbol{k}, \tag{1}$$

$$\frac{D\Theta'}{Dt} = -\boldsymbol{u}\cdot\nabla\Theta_a - \frac{\Theta'}{\tau}, \tag{2}$$

$$\nabla\cdot(\rho_o\boldsymbol{u}) = 0. \tag{3}$$

Here, $\boldsymbol{u}$ represents the fluid velocity, $\Theta \equiv \Theta' + \Theta_a$ is the potential temperature (equivalent to the specific entropy since $ds = c_p d\ln\Theta$, with c_p the specific heat at constant pressure), and $\pi' \equiv p'/\rho_o$ is a density-normalized pressure perturbation. The *reference* state about which the anelastic asymptotic expansion is constructed is denoted by the subscript "o". It is taken as isentropic ($\Theta_o = $ constant) and in hydrostatic balance, with $g(r) = g_b(r_b/r)^{-2}$, the radially diminishing magnitude of the gravitational acceleration, pointing in the negative unit vector direction $\boldsymbol{k}$. The reference state is constructed using values for temperature T_b, density ρ_b, and gravitational acceleration g_b at the base of the domain obtained from a solar structure model (Christensen-Dalsgaard et al. 1996).

Primes in Equations (1) and (2) denote perturbations with respect to an imposed *ambient* state (indicated with subscript "a"). The ambient state is chosen to represent the large-scale thermodynamic equilibrium structure of the Sun on timescales much longer than the convective turnover time τ_c. The

Newtonian cooling term, $-\Theta'/\tau$, in (2) relaxes the potential temperature to that of the ambient state over a timescale $\tau \gg \tau_c$. Thus, the ambient entropy stratification of the domain is maintained over long timescales, limiting restratification by the convection and driving motions in regions of ambient state superadiabaticity. This is a common approach in atmospheric models when addressing evolutionary fluctuations about large-scale equilibria (Smolarkiewicz et al. 2001; Grabowski & Smolarkiewicz 2002; Warn-Varnas et al. 2007) and has also been employed in some previous simulations of global solar magnetoconvection (Ghizaru et al. 2010; Racine et al. 2011; Cossette et al. 2013).

In detail, we construct the ambient state to be strongly subadiabatic in the lower portion of the computational domain $r_b \leqslant r < r_i$, with $r_i = 0.718\,R_\odot$, adiabatic in the bulk $r_i \leqslant r \leqslant r_s$, and superadiabatic above $r_s < r \leqslant r_t$. It satisfies the polytropic equations for an ideal gas, $p_a = K\rho_a^{1+1/m}$, $p_a = \rho_a R T_a$, and $dp_a/dr = -\rho_a g$ with a prescribed polytropic index $m = m(r)$. In the subadiabatic lower portion of the domain, the polytropic index m decreases linearly from $m_b = 3.0$ at the base to $m_i = m_{\rm ad} = 3/2$ at $r = r_i$. It then remains constant at its adiabatic value through the bulk of the domain, before being set to a superadiabatic value $m_s < m_{\rm ad}$ above $r = r_s$. The ambient potential temperature profile for each run is then $\Theta_a \equiv T_a(\rho_b T_b/\rho_a T_a)^{1-1/\gamma}$.

The relaxation time to the ambient state is set to $\tau = 20$ solar days in the stably stratified and superadiabatic regions and $\tau = 1000$ solar days in the adiabatic bulk of the domain. It is important to note that while we call the bulk of the domain adiabatic, this is a statement about the ambient state only. The long relaxation time in that portion of the domain allows the convection to reconfigure the thermodynamic gradients therein. This allows us to study how the interior of the convection zone evolves when subject to strong surface driving and how this in turn effects the spectrum of the motions that ensue. As a control experiment, we also consider a simulation for which the ambient state is subadiabatic in the lower portion $r_b \leqslant r < r_i$ (as described above) but weakly superadiabatic across the remainder of the domain $r_i \leqslant r < r_t$. The relaxation time in that case is taken to be 20 solar days throughout.

Integration of Equations (1)–(3) is carried out with the hydrodynamic solver of the magnetohydrodynamic EULAG model (Prusa et al. 2008; Smolarkiewicz & Charbonneau 2013). EULAG employs a non-oscillatory forward-in-time advection operator (Smolarkiewicz 2006), allowing stable integration of the equations with all dissipation delegated to the advection scheme's truncation terms (Smolarkiewicz & Prusa 2002). We examine a Cartesian domain extending from $r_b = 0.63\,R_\odot$ to $r_t = 0.965\,R_\odot$ in solar radius, with physical dimensions $910.53\,{\rm Mm} \times 910.53\,{\rm Mm} \times 227.63\,{\rm Mm}$ on a grid of $1024^2 \times 256$ points. The reference state is characterized by density scale-height $H_\rho = 360$ km at the surface and 85 Mm at the base of the convection zone, spanning a total of 11 scale heights across the domain. Nonuniform gridding in the vertical direction accommodates the rapidly decreasing density scale-height near the top of the domain (Prusa & Smolarkiewicz 2003). The domain is horizontally periodic, with vanishing vertical velocity and zero radial flux of momentum and potential temperature imposed at both upper and lower boundaries.
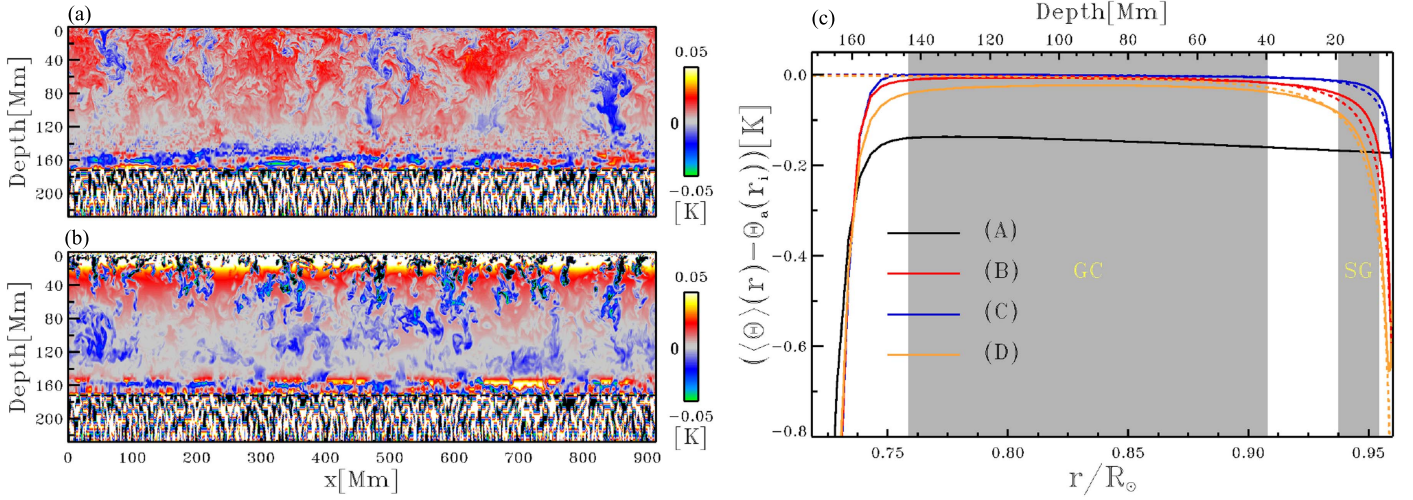
Figure 1. Vertical cross-sections of the instantaneous deviations $\widetilde{\Theta} \equiv \Theta - \langle\Theta\rangle$ from the horizontal mean of the potential temperature $\langle\Theta\rangle$ taken from case A (panel (a)) and B (panel (b)) at $t = 10$ solar days. Case A is characterized by a weakly superadiabatic ambient profile ($m_s = 1.4999998$) across the convection zone ($r_t \geqslant r \geqslant r_i$), whereas Case B uses a strictly adiabatic profile in the region ($r_s \geqslant r \geqslant r_i$, $r_s \equiv 0.96\,R_\odot$) and a superadiabatic profile ($m_s = 1.4994$) inside a 3.5 Mm deep region below the surface ($r_t \geqslant r \geqslant r_s$). The horizontal dashed line denotes the location of the interface at $r = r_i$. Low-entropy fluid parcels produced in the driven region pass through the convection zone and impact the stable layer below, exciting gravity waves there. Panel (c) shows profiles of $\langle\Theta(r)\rangle - \Theta_a(r_i)$ for each case in the region $r_s \geqslant r \geqslant r_i$ (solid lines). As in Case B, Cases C and D employ strictly adiabatic ambient profiles below $r_s = 0.96\,R_\odot$ and superadiabatic profiles characterized by $m_s = 1.49985$ and $m_s = 1.4985$ above, respectively. Shaded areas labeled "GC" and "SG" correspond to depth ranges over which $100\,\text{Mm} < 4H_\rho < 300\,\text{Mm}$ and $20\,\text{Mm} < 4H_\rho < 50\,\text{Mm}$, respectively. The change in $\langle\Theta\rangle$ near the surface in Cases B–D is well reproduced by cold fluid parcels moving down adiabatically from $r = r_s$ (dashed lines). The subadiabatic stratification at the base of the convection zone is caused by the accumulation of low-entropy fluid there, taking place on a timescale $\langle\Theta'\rangle(d\langle\Theta'\rangle/dt)^{-1} \gtrsim 20$ solar days.

3. RESULTS

First, we compare two simulations that share approximately the same total kinetic energies and convective fluxes in the bulk of the convection zone. In Case A we specify a weakly superadiabatic ambient state across the full depth of the convection zone, while in Case B the superadiabatic ambient state is confined to the upper 3.5 Mm of the domain spanning 5 density scale-heights (hereafter the cooling layer). The cooling layer is in some ways analogous to the solar photosphere, where the spatial scale of the granular downflows is set by the local density scale-height. The typical spatial scale of the low-entropy parcels generated in the cooling layer of Case B similarly reflects the turbulent energy injection scale $L \sim 4H_\rho$ ($H_\rho \sim 0.36$–2.6 Mm) there (Rincon 2007; Lord et al. 2014). Note that the cooling layer is distinct from the superadiabatic region that we will see develops below it as a result of the flow itself and determines the spectrum of larger-scale motions.

The flow in Case A is dominated by larger-scale motions than in Case B (Figure 1) and positive entropy perturbations that, although weaker, tend to be coherent over the full depth of the convection zone. The mean thermodynamic stratification (Figure 1(c)) in Case A is characterized by a weakly superadiabatic mean state ($d\langle\Theta\rangle/dr < 0$) throughout. The mean stratification in Case B, on the other hand, is very close to adiabatic throughout the bulk, but strongly superadiabatic immediately below the cooling layer. The turbulent energy injection scale in that region is comparable to the size of supergranules (region SG in Figure 1(c)), and the buoyancy forces therein drive upflows on that scale (red and yellow areas in Figure 1(b)). In Case A, on the other hand, the convectively unstable mean stratification through the bulk of the convection zone ("GC" region in Figure 1(c)) additionally drives giant-cell scale motions. We note that these simulations are not strictly in equilibrium. Both the superadiabatic stratification in the upper layers and the subadiabatic region at the base of the convection
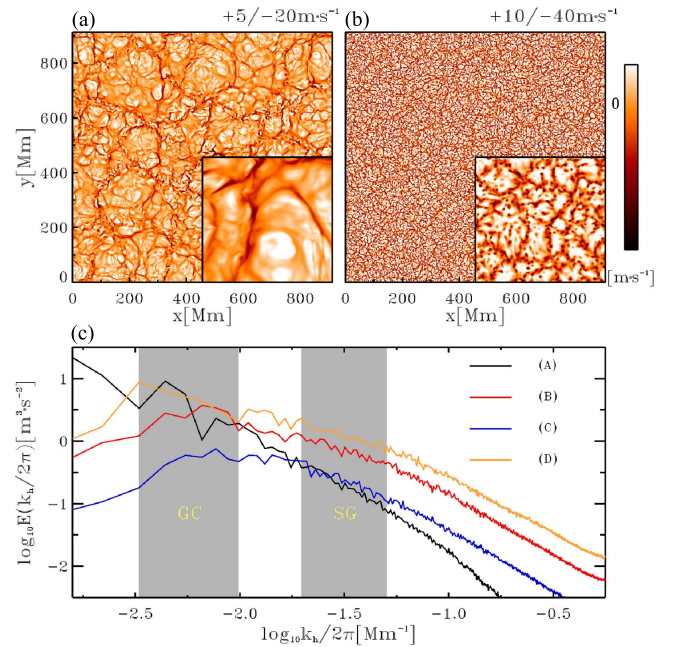

Figure 2. Horizontal cross-sections of the instantaneous vertical velocity u_r taken at 5 Mm depth corresponding to Cases A (panel (a)) and B (panel (b)) at $t = 10$ solar days. The inserted plot in each panel shows the magnified view of a $100\,\text{Mm}^2$ area. As in other experiments of compressible convection, u_r is characterized by broad upflows surrounded by a network of narrow downflow lanes (see Nordlund et al. 2009; Miesch & Toomre 2009 and references therein). Panel (c): instantaneous horizontal velocity power spectra taken at 5 Mm depth for each case. Here, $k_h \equiv 2\pi/\lambda$, with λ the horizontal wavelength. Shaded areas labeled "GC" and "SG" correspond, respectively, to spectral ranges where $100\,\text{Mm} < \lambda < 300\,\text{Mm}$ (hereafter giant cells) and $20\,\text{Mm} < \lambda < 50\,\text{Mm}$ (hereafter supergranular scales).

zone are evolving, but this occurs on timescales much longer than the convective turnover time so the consequent spectra of interest (Figure 2) are nearly stationary.

Table 1
Relationship between the Horizontal Power Distribution at 5 Mm Depth and the Superadiabaticity of the Convection Zone

Case	P_G	P_S	P_S/P_G	ϵ_G [$\times 10^{-8}$]	ϵ_S [$\times 10^{-8}$]	KE_h	F_e
A	1.0000	1.0000	0.2241	−1.68	−0.25	1.00	1.00
B	0.7082	3.5573	1.1255	−0.86	−11.1	1.00	92.93
C	0.1385	1.1654	1.8857	−0.23	−3.0	0.28	18.31
D	1.2807	6.0726	1.0625	−1.15	−20.6	1.86	157.47

Note. Second and third columns show, respectively, the total power contained in giant cells (P_G) and supergranular scales (P_S) relative to that of case A, with the fourth column showing the ratio of supergranular to giant-cell power. Fifth and sixth columns display, respectively, the maximal value of the superadiabaticity parameter $\epsilon \equiv H_T/\Theta_o d \langle \Theta \rangle /dr$ inside driving regions corresponding to giant cells (100 Mm < $4H_\rho$ < 300 Mm) and supergranular scales (20 Mm < $4H_\rho$ < 50 Mm), with $H_T \equiv -(d \ln T_o/dr)^{-1}$ the temperature scale-height. The seventh and eighth columns show, respectively, the ratio of total kinetic energies associated with the horizontal flow component and enthalpy fluxes relative to case A at 5 Mm Depth.

These spectra reflect the mean entropy profiles achieved. In Case A, the mean profile is maintained by relaxation to the ambient state, but in Cases B (also C and D below), the relaxation time is too long in the region below the cooling layer to be important. The strongly superadiabatic region below the cooling layer in Case B is caused by the presence of the cool downflowing plumes that change the mean state, driving the upflows. The importance of the downflows decreases with depth because their contribution to $\langle \Theta \rangle$ decreases with increasing density until negligible. In a strictly adiabatic background, the downflow contribution decreases as $\rho_0(r_s)/\rho_0(r)$, even in the presence of entrainment, since the entrained fluid has $\Theta' = 0$ and thus merely dilutes. The change in $\langle \Theta \rangle$ is then well approximated (*dashed* curves in Figure 1(c)) by parcels moving adiabatically downward so that $\langle \Theta(r) \rangle - \Theta_a(r_i) \approx f(r)\Theta_d$, where $f(r) \equiv f_d \rho_o(r_s)/\rho_o(r)$ and Θ_d and f_d are the downflowing fluid's average potential temperature and filling factor at the height $r = r_s$ where it originates. To illustrate this further, we consider additional experiments with different values of the polytropic index in the cooling layer (Cases C and D in Figure 1(c)). Parcels in Cases B–D originate from the same depth (cooling layers have the same thickness) but possess different initial entropy fluctuations. The larger the initial entropy fluctuations, the smaller $f(r)$ must become before the downflow contribution to the mean state becomes negligible, hence the increase of the extent of the superadiabatic region in Case B compared to C and in Case D compared to B.

This explanation for the mean state profile relies on the adiabatic transit of the downflow plumes across the domain. The transit time τ_t of the cool plumes across the simulated domain ($\tau_t \approx 1$ solar day) is shorter than the time it takes for a parcel to diffuse (numerically). In the Sun, radiative diffusion dominates, with estimates for the diffusivity κ ranging from about 10^5 to 10^7 cm^2 s^{-1} across the solar convection zone (Miesch 2005). The characteristic diffusion timescale $\tau_d \sim l^2/\kappa$ of a plume with spatial scale $l \sim 300$ km (i.e., the thickness of the radiative boundary layer at the photosphere) is thus between 3 and 285 years. Assuming that the transit time τ_t of cold plumes generated at the photosphere is of the order of the turnover time of the largest convective cells (∼1 month), $\tau_t \ll \tau_d$. Solar plumes may thus be expected to behave as in Cases B–D, traveling across the convection zone without exchanging a significant amount of heat with the surrounding medium. The consequent superadiabatic mean solar stratification is then due only to the plumes' presence and their geometry as they move across layers of increasing density. This implies that the interior stratification of the Sun could be

extremely close to adiabatic with a relatively thin superadiabatic layer determined by the thermodynamic properties of the granular downflows in the upper layers.

The characteristic scales of the convective flows in our solutions reflect the depth of the superadiabatic region induced by the downflows descending from the cooling layer. Cell diameters in Case A are much larger than in Case B, with 200 Mm scales typical in Case A and smaller 40 Mm scales in Case B (Figures 2(a) and (b)). This is reflected in the horizontal velocity power spectra (Figure 2(c)). At 5 Mm depth, the areas under spectra A and B (Table 1) are the same, but the power in supergranular scales in Case B exceeds that in Case A. The opposite is true of the power at the largest giant-cell scales. Increasing the polytropic index m_s in the cooling layer of Case C decreases the power at all scales relative to Case B, while decreasing it in Case D increases the amplitude of the convective motions (Figure 2(c)). An increase of power due to the intensification of convective driving is accompanied by an increase in the spatial extent of the superadiabatic region below the surface (Figure 1(c)) and the superadiabaticities ϵ_G and ϵ_S inside the giant-cell and supergranular driving regions, as summarized in Table 1. Likewise, the correlation between the enthalpy flux F_e and ϵ_S reflects the increase of convective driving below. What is most important in these results is that the ratio of supergranular to giant-cell power (P_S/P_G) correlates with the characteristic depth of the superadiabatic region.

4. SUMMARY AND REMARKS

These experiments demonstrate that in surface-driven convection the depth of the transition to a nearly adiabatic interior reflects the presence of the adiabatically descending downflowing plumes and is thus proportional to their initial density and entropy contrast. If this is true of the solar convection zone, then the mean stratification in its upper layers is determined by simple dilution of the granular downflows, and the solar supergranular scale is determined by the scale height at the depth at which their contribution to the mean becomes negligible. The transition to an isentropic mean is likely very shallow in the Sun because of the low photospheric density where the granular downflows originate and the rapid increase of mean density with depth. The ratio of power at supergranular to giant-cell scales reflects this, increasing in the simulations with shallower transition depth.

The short transit time of the cold downflowing plumes across the solar convection zone compared to the characteristic timescale of radiative heating suggests that the convective heat transport is highly nonlocal (e.g., Rieutord & Zahn 1995;

Spruit 1997; Brandenburg 2015) and diffusive effects are negligible. The analysis presented in this work dealt only with one aspect of that transport, the change in the mean stratification and consequent convective driving resulting from downflowing plumes generated in a shallow cooling layer. It did not address the origin of the initial adiabatic stratification or the steady state possibly achievable if heating of the fluid in the overshoot layer exactly matches the cooling above. Future experiments that include self-consistent heat transfer between the top and bottom boundaries are required to assess the viability of such strictly nonlocal transport in the context of a thermally equilibrated star.

REFERENCES

Berrilli, F., Del Moro, D., Russo, S., Consolini, G., & Straus, T. 2005, ApJ, 632, 677

Berrilli, F., Scardigli, S., & Giordano, S. 2013, SoPh, 282, 379

Brandenburg, A. 2015, ApJ, in press (arXiv:1504.03189)

Cattaneo, F., Lenz, D., & Weiss, N. 2001, ApJL, 563, L91

Christensen-Dalsgaard, J., Dappen, W., Ajukov, S. V., et al. 1996, Sci, 272, 1286

Cossette, J.-F., Charbonneau, P., & Smolarkiewicz, P. K. 2013, ApJL, 777, L29

Crouch, A. D., Charbonneau, P., & Thibault, K. 2007, ApJ, 662, 715

Duvall, T. L., Jr., & Birch, A. C. 2010, ApJL, 725, L47

Featherstone, N. A., & Hindman, B. W. 2016, ApJ, 818, 32

Featherstone, r. A., & Miesch, M. S. 2015, ApJ, 804, 67

Gastine, T., Wicht, J., & Aurnou, J. M. 2013, Icar, 225, 156

Ghizaru, M., Charbonneau, P., & Smolarkiewicz, P. K. 2010, ApJL, 715, L133

Goldbaum, N., Rast, M. P., Ermolli, I., Sands, J. S., & Berrilli, F. 2009, ApJ, 707, 67

Grabowski, W. W., & Smolarkiewicz, P. K. 2002, MWRv, 130, 939

Greer, B. J., Hindman, B. W., Featherstone, N. A., & Toomre, J. 2015, ApJL, 803, L17

Hanasoge, S., Gizon, L., & Sreenivasan, K. R. 2016, AnRFM, 48, 191

Hanasoge, S. M., Duvall, T. L., & Sreenivasan, K. R. 2012, PNAS, 109, 11928

Hanasoge, S. M., Duvall, T. L., Jr., & DeRosa, M. L. 2010, ApJL, 712, L98

Hathaway, D. H., Beck, J. G., Bogart, R. S., et al. 2000, SoPh, 193, 299

Hathaway, D. H., Teil, T., Norton, A. A., & Kitiashvili, I. 2015, ApJ, 811, 105

Hathaway, D. H., Upton, L., & Colegrove, O. 2013, Sci, 342, 1217

Hotta, H., Rempel, M., & Yokoyama, T. 2015, ApJ, 803, 42

Leighton, R. B., Noyes, R. W., & Simon, G. W. 1962, ApJ, 135, 474

Leitzinger, M., Brandt, P. N., Hanslmeier, A., Pötzi, W., & Hirzberger, J. 2005, A&A, 444, 245

Lipps, F. B., & Hemler, R. S. 1982, JAtS, 39, 2192

Lord, J. W., Cameron, R. H., Rast, M. P., Rempel, M., & Roudier, T. 2014, ApJ, 793, 24

Miesch, M. S. 2005, LRSP, 2, 1

Miesch, M. S., Brun, A. S., De Rosa, M. L., & Toomre, J. 2008, ApJ, 673, 557

Miesch, M. S., & Toomre, J. 2009, AnRFM, 41, 317

Nordlund, Å., Stein, R. F., & Asplund, M. 2009, LRSP, 6, 2

November, L. J. 1989, ApJ, 344, 494

November, L. J., Toomre, J., Gebbie, K. B., & Simon, G. W. 1981, ApJL, 245, L123

O'Mara, B., Miesch, M. S., Featherstone, F. A., & Augustson, K. C. 2016, AdSpR, 58, 1475

Prusa, J. M., Smolarkiewicz, P. K., & Wyszogrodzki, A. A. 2008, CF, 37, 1193

Prusa, M. P., & Smolarkiewicz, P. K. 2003, JCoPh, 190, 601

Racine, É., Charbonneau, P., Ghizaru, M., Bouchat, A., & Smolarkiewicz, P. K. 2011, ApJ, 735, 46

Rast, M. P. 2003, ApJ, 597, 1200

Rast, M. P., & Toomre, J. 1993, ApJ, 419, 224

Rieutord, M., Roudier, T., Malherbe, J. M., & Rincon, F. 2000, A&A, 357, 1063

Rieutord, M., & Zahn, J.-P. 1995, A&A, 296, 127

Rincon, F. 2007, in Proc. IAU Symp. 239, Convection in Astrophysics, ed. F. Kupka, I. Roxburgh, & K. Chan (Cambridge: Cambridge Univ. Press), 58

Roudier, T., Rieutord, M., Malherbe, J. M., et al. 2012, A&A, 540, A88

Simon, G. W., & Leighton, R. B. 1964, ApJ, 140, 1120

Smolarkiewicz, P. K. 2006, IJNMF, 50, 1123

Smolarkiewicz, P. K., & Charbonneau, P. 2013, JCoPh, 236, 608

Smolarkiewicz, P. K., Margolin, L. G., & Wyszogrodzki, A. A. 2001, JAtS, 58, 349

Smolarkiewicz, P. K., & Prusa, J. M. 2002, IJNMF, 39, 799

Spruit, H. 1997, MmSAI, 68, 397

Thompson, M. J., Christensen-Dalsgaard, J., Miesch, M. S., & Toomre, J. 2003, ARA&A, 41, 599

Warn-Varnas, A., Hawkins, J., Smolarkiewicz, P. K., et al. 2007, OcMod, 18, 97